ChemComm

COMMUNICATION

View Article Online
View Journal

Cite this: DOI: 10.1039/d6cc00778c

Received 5th February 2026,
Accepted 2nd March 2026

DOI: 10.1039/d6cc00778c

rsc.li/chemcomm

Selective etching of binary nanoparticle superlattices *via* thermally induced asymmetric ligand evolution

Di Lei,[a] Hao Wang,[a] Ting Wang,[a] Fangyue Wu,[a] Ning Ding,[a] Yajun Wang,*[b] Tongtao Li*[a] and Angang Dong *[a]

We report a method to selectively etch either component in $NaYF_4/Fe_3O_4$ binary nanoparticle superlattices using a single etchant. Thermally-induced evolution of oleate ligands on the $NaYF_4$ nanoparticles reverses their relative etching susceptibility in oxalic acid, yielding non-close-packed nanoparticle arrays with tunable architectures.

The self-assembly of colloidal nanoparticles (NPs) provides a powerful bottom-up route to organize nanoscale building blocks into ordered superlattices with collective and emergent properties. Such superlattices have attracted intense interest for applications in electronic, optical, and mechanical properties, where long-range periodicity and structural coherence are essential.[1–3] Importantly, the properties of these materials can be precisely tuned by the choice and number of NP building blocks, the length and functionality of the surface ligands, and the symmetry that governs their coupling within the lattice.[4]

Beyond conventional close-packed architectures, non-close-packed (NCP) ordered arrays—in which NPs remain periodically arranged but are separated by larger, well-defined distances—offer distinct advantages, including enhanced accessibility, porosity and electromagnetic field concentration. These features make NCP arrays particularly attractive as surface-enhanced Raman scattering (SERS) substrates[5] and as templates for quantum dot or plasmonic device fabrication.[6] Despite several elegant demonstrations based on highly specific interactions or finely balanced assembly conditions,[7] a general and programmable strategy to access ordered NCP NP arrays is still lacking.

Selective removal of one component from binary NP superlattices (BNSLs) by chemical etching represents a particularly powerful route to transform dense arrays into ordered NCP architectures. In practice, however, most reported strategies rely on the intrinsic chemical differences between the two components and require the use of different etchants to achieve selectivity.[5,8] A representative example is reported in Fe_3O_4/Au BNSLs, where Fe_3O_4 NPs are etched by acids while Au NPs require a cyanide solution such as KCN.[5] Although effective, this etchant-dependent paradigm is inherently complex, limits programmability, and offers little insight into the molecular origin of etching selectivity. A simpler and mechanistically transparent strategy that enables selective etching using a single etchant—while retaining full structural order—therefore remains highly desirable for post-assembly structural editing.

Here we introduce an alternative, ligand reorganization–governed strategy for selective etching of BNSLs using a single etchant. Using a $NaYF_4/Fe_3O_4$ system, we exploit the thermally induced chemical transformation and crosslinking of oleate ligands on $NaYF_4$ NPs, enabled by their low thermal conductivity and nanoscale heat accumulation under thermal treatment.[9] As a result, the ligand shell on $NaYF_4$ evolves from a loosely bound molecular layer into a rigid, interconnected network. When the degree of ligand crosslinking is low, $NaYF_4$ remains susceptible to etching in oxalic acid; when crosslinking is sufficiently developed, acid penetration is effectively suppressed. In contrast, the ligand shell on the Fe_3O_4 NPs remains largely unchanged under the same conditions. This difference allows the relative etching susceptibility of the two components to be reversed simply by tuning the thermal treatment time, without changing the etching chemistry. Spectroscopic analyses reveal a molecular-level reconstruction of the ligand shell as the origin of this behavior, establishing a new conceptual basis for programmable post-assembly structural editing of nanocrystal superlattices.

Monodisperse $NaYF_4$ and Fe_3O_4 nanospheres (NSs) were synthesized following established protocols.[10] For constructing AB-type BNSLs, Fe_3O_4 NSs (diameter: 13.1 ± 0.3 nm) and $NaYF_4$ NSs (diameter: 33.7 ± 0.1 nm) were co-assembled at the liquid–air interface *via* slow evaporation of hexane (Fig. S1a and c).[11] This process yields two-dimensional membranes with long-range order, which can be readily transferred onto carbon-coated transmission electron microscopy (TEM) grids for structural characterization and post-assembly processing (Fig. 1a). Low-magnification TEM

[a] *Department of Chemistry and Shanghai Key Laboratory of Molecular Catalysis and Innovative Materials, Fudan University, Shanghai 200433, China. E-mail: ttli@fudan.edu.cn, agdong@fudan.edu.cn*
[b] *College of Chemistry and Materials Engineering, Wenzhou University, Wenzhou 325027, China. E-mail: yajunwang@wzu.edu.cn*

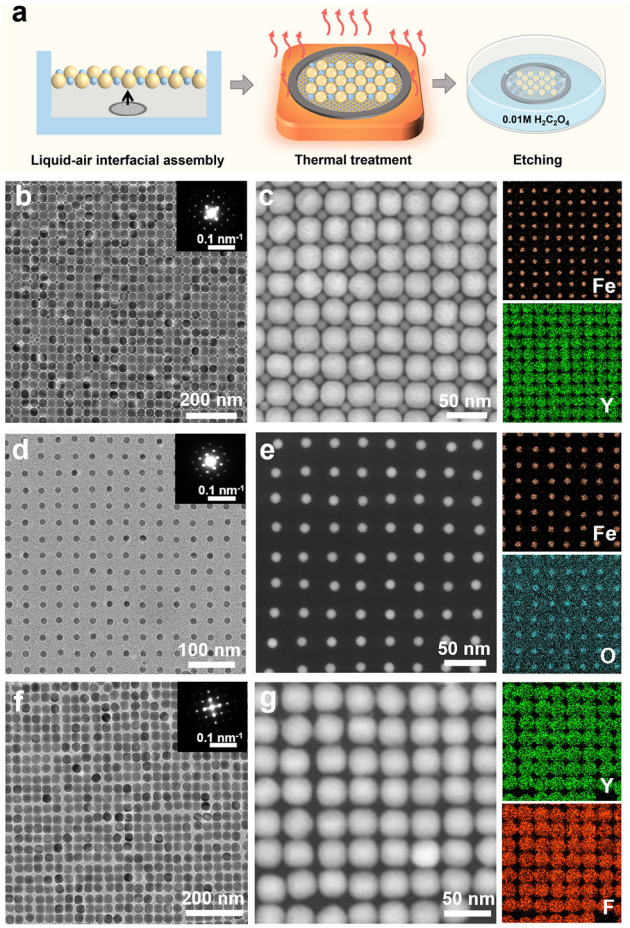

Fig. 1 (a) Schematic illustration of the method. (b) TEM image, SAED pattern (inset), and (c) HAADF-STEM image and elemental mappings of AB-type BNSLs assembled from $NaYF_4$ and Fe_3O_4 NSs. (d) TEM image and (e) HAADF-STEM image and corresponding elemental mappings of an NCP Fe_3O_4 array. (f) TEM image, (g) HAADF-STEM image, and corresponding elemental mappings of an NCP $NaYF_4$ array.

images reveal long-range periodic ordering of the AB-type superlattice (Fig. 1b and Fig. S3), while the corresponding small-angle electron diffraction (SAED) pattern confirms crystalline coherence across the entire lattice. High-angle annular dark-field scanning TEM (HAADF-STEM) images combined with elemental mapping unambiguously assign Fe and Y to two interpenetrating sublattices, verifying the formation of a binary array (Fig. 1c).

By adjusting the thermal treatment time prior to etching, the target of oxalic acid etching can be reversibly switched. After a short duration of thermal treatment (3 h), $NaYF_4$ is preferentially removed due to its intrinsically lower acid resistance compared with Fe_3O_4 (Fig. S4), yielding an NCP Fe_3O_4 array. Large-area TEM images show a periodic square array (Fig. 1d), while HAADF-STEM and Fe/O elemental mapping confirm the exclusive retention of Fe_3O_4 in the remaining lattice (Fig. 1e). The average diagonal center-to-center spacing is 36.6 nm (Fig. S5), consistent with the diameter of the removed $NaYF_4$ NSs plus the oleate ligand shell. Both the particle size and lattice registry of Fe_3O_4 remain unchanged, indicating that oxalic acid selectively removes $NaYF_4$ without disrupting the Fe_3O_4 sublattice.

Conversely, extending the thermal treatment to 6 h reverses the etching selectivity. Under identical oxalic acid conditions, Fe_3O_4 NSs are now preferentially removed, while $NaYF_4$ NSs remain intact, producing a complementary NCP $NaYF_4$ array. Low-magnification TEM images confirm the formation of an ordered $NaYF_4$ array (Fig. 1f and Fig. S6), and HAADF-STEM with Y/F elemental mapping verifies the exclusive presence of $NaYF_4$ NSs in the remaining lattice (Fig. 1g). Notably, the etching process is not instantaneous but evolves progressively with time: statistical TEM analysis after 3 h and 6 h of thermal treatment reveals a continuous, stepwise removal of the susceptible component until complete elimination is achieved (Fig. S7). This inversion of etching susceptibility establishes an "alternative etching" regime governed solely by the thermal treatment time of the superlattice, rather than by changing the chemical identity of the etchant.

To rationalize the "alternative etching" behavior observed in Fig. 1, we quantified the time required for complete removal of $NaYF_4$ and Fe_3O_4 NSs as a function of prior thermal treatment (Fig. 2a). The etching kinetics of Fe_3O_4 are largely insensitive to the thermal treatment time, whereas the etching kinetics of $NaYF_4$ increase systematically with increasing thermal treatment duration. The plot reveals a crossover at 4 h, where the relative etching susceptibility of the two components is reversed. Without thermal treatment, $NaYF_4$ is etched much faster than Fe_3O_4 and the superlattice collapses during etching (Fig. S4). A moderate treatment of 3 h stabilizes the lattice while maintaining preferential removal of $NaYF_4$, yielding intact Fe_3O_4 NCP arrays. Extending the thermal treatment to 6 h drives the system beyond the crossover, where Fe_3O_4 is preferentially etched and the $NaYF_4$ sublattice remains intact. This inversion originates from the intrinsic difference in thermal conductivity between the two cores, which leads to programmable modification of the surface states. We therefore probe the molecular origin of this behavior by examining how thermal treatment reconstructs the ligand shells of both components.

To elucidate the molecular origin of the thermally induced etching reversal, we first investigated the evolution of surface ligands on $NaYF_4$ NSs by ^{1}H nuclear magnetic resonance (NMR) spectroscopy. The ligand structures were analyzed using single-component $NaYF_4$ samples subjected to different thermal treatments (0 h and 6 h), with spectra acquired in $CDCl_3$ after redispersing the thermally treated NSs from silicon substrates (Fig. 2b and Fig. S8). The ^{1}H NMR spectrum of the as-prepared $NaYF_4$ NSs shows characteristic signals of oleate ligands. After 6 h thermal treatment, the alkene resonance at δ = 5.34 ppm, assigned to –HC═CH– protons, disappears completely, indicating cleavage of the C═C bond in surface-bound oleate.[12,13] This transformation enables ligand crosslinking and shell densification, forming a compact surface layer that suppresses acid penetration and underlies the enhanced etching resistance.

Fourier transform infrared (FTIR) spectroscopy reveals a pronounced reorganization of the ligand shell on $NaYF_4$ NSs upon thermal treatment. As shown in Fig. 2c and d, pristine $NaYF_4$ NSs exhibit characteristic oleate features, including CH_2 stretching bands at 2924 and 2854 cm^{-1} and a weak ═C–H vibration at 3007 cm^{-1}, consistent with surface-bound oleic acid ligands. After thermal treatment, the most pronounced

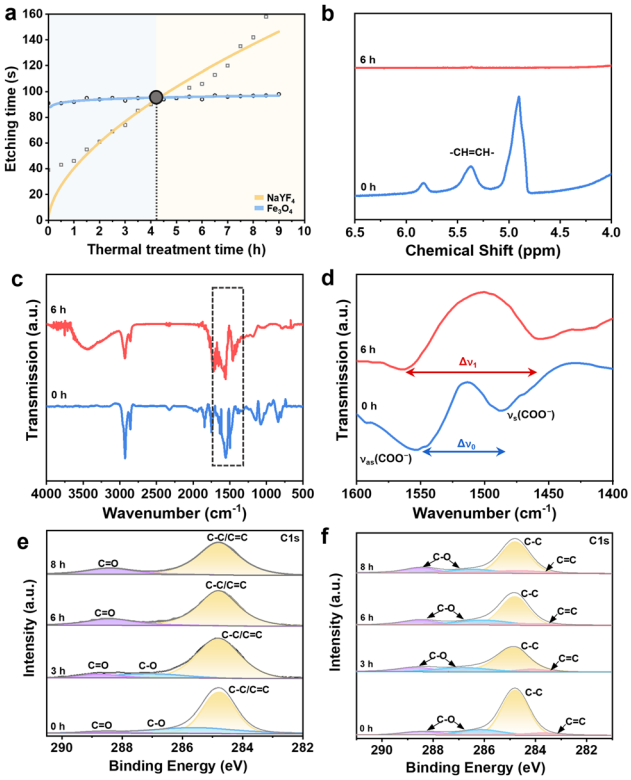

Fig. 2 (a) Plot of the time required for complete dissolution of $NaYF_4$ and Fe_3O_4 NSs as a function of thermal treatment duration. (b) Expanded ^1H NMR spectra of the $NaYF_4$ NSs. (c) FTIR spectra and (d) expanded FTIR spectra of the $NaYF_4$ NSs. (e) and (f) C 1s XPS spectra of the $NaYF_4$ and Fe_3O_4 NSs, respectively.

changes occur in the carboxylate region. In the pristine sample, the bands at 1550 and 1485 cm^{-1} are associated with the asymmetric (ν_{as}) and symmetric (ν_s) stretching vibrations of the carboxylic group of the bound oleic acid. After thermal treatment, these bands shift to 1562 and 1457 cm^{-1}. Accordingly, the separation $\Delta\nu = \nu_{as} - \nu_s$ increases from 65 cm^{-1} to 105 cm^{-1}.[14–16] Fig. S9 shows the FTIR spectra of $NaYF_4$ NSs following thermal treatment for different durations (0, 3, 6 and 8 h). With increasing annealing time, the ν_{as} band gradually shifts to higher wavenumbers, whereas the ν_s band moves to lower wavenumbers, leading to a progressive increase in $\Delta\nu$. Such an increase in $\Delta\nu$ is commonly associated with a change in the carboxylate coordination environment, consistent with a transition from relatively flexible surface binding to a more compact and constrained coordination state. This evolution suggests that thermal treatment induces chemical reorganization and intermolecular coupling of oleate ligands on the $NaYF_4$ surface.

X-ray photoelectron spectroscopy (XPS) provides direct evidence for thermally induced ligand reconstruction on $NaYF_4$ NSs and highlights its contrast with Fe_3O_4 NSs. In the C 1s spectra of $NaYF_4$ (Fig. 2e), thermal treatment induces a systematic decrease of the C–O component accompanied by an increase of the C=O contribution, which supports the formation of a more chemically constrained surface layer that correlates with the enhanced acid resistance of $NaYF_4$ after thermal treatment. In contrast, the C 1s spectra of Fe_3O_4 NSs (Fig. 2f) show no signatures of ligand crosslinking under the same thermal treatment. Simultaneously, the Fe $2p_{3/2}$ and Fe $2p_{1/2}$ peaks (Fig. S10c) shift slightly toward higher binding energies after thermal treatment, indicating partial oxidation of Fe^{2+} to Fe^{3+}.[3,6] Thus, Fe_3O_4 primarily undergoes core-level oxidation rather than surface–ligand reconstruction. This stark difference demonstrates that only $NaYF_4$ experiences thermally driven ligand reorganization and densification, providing the molecular basis for the programmable and reversible etching selectivity observed in the binary superlattices.

The spectroscopic evidence and etching trends in Fig. 2 converge on a unified mechanism: nanoscale heat accumulation in $NaYF_4$ NSs triggers ligand intermolecular crosslinking and densification of the oleate shell, transforming a permeable organic corona into a compact barrier against acid attack.[9] The surface ligands on the Fe_3O_4 NSs, in contrast, do not undergo comparable reconstruction under the same thermal conditions and remain relatively accessible to the etchant.[3,6] The thermal conductivity of $NaYF_4$ (0.5 W m^{-1} K^{-1}), markedly lower than that of Fe_3O_4 (6 W m^{-1} K^{-1}), results in preferential heat localization during thermal treatment.[17,18] This divergence defines the molecular origin of the programmable and reversible etching selectivity in the binary superlattices.

Crucially, this asymmetric ligand evolution arises from the intrinsic difference in thermal conductivity and heat dissipation between the two inorganic cores, which dictates how efficiently thermal energy is delivered to the surface ligands. As schematically illustrated in Fig. 3, the superlattice therefore encodes a thermally programmable surface chemistry: at short thermal treatment times $NaYF_4$ is preferentially etched, whereas prolonged thermal treatment renders $NaYF_4$ acid-resistant and shifts the etching to Fe_3O_4. In this way, thermal treatment time is translated into controllable interfacial reactivity, enabling reversible switching of etching selectivity by engineering ligand-shell evolution rather than altering the etchant itself.

To evaluate the generality of the ligand-reorganization–governed etching mechanism, we extended this strategy to a second binary system composed of nanodumbbells (NDS) and NSs (Fig. 4a).[10] Oleate-capped β-$NaYF_4$:Yb/Er@$NaGdF_4$@$NaNdF_4$ NDs, defined by the diagonal head size (D) and waist diameter (d) (Fig. S2), were co-assembled with Fe_3O_4 NSs (21.1 ± 0.1 nm; Fig. S1b) using the same liquid–air interfacial method. The two components organize into a hexagonal AB_2-type superlattice, in

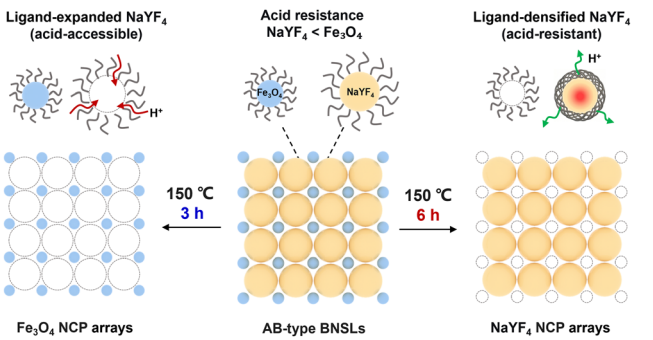

Fig. 3 Schematic illustrating the inversion of etching selectivity in binary superlattices.

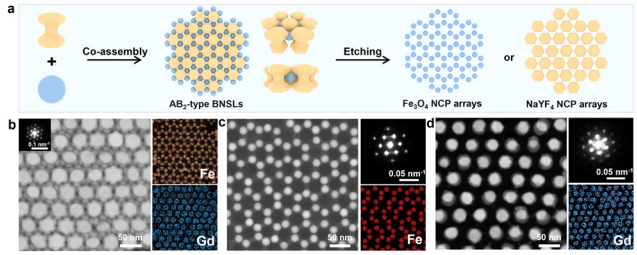

Fig. 4 (a) Schematic of the assembly and selective etching of AB_2-type superlattices formed from β-$NaYF_4$:Yb/Er@$NaGdF_4$@$NaNdF_4$ NDs and Fe_3O_4 NSs. (b) HAADF-STEM image (inset: SAED pattern) and corresponding elemental mappings of the AB_2-type superlattices. (c) HAADF-STEM image of the honeycomb-packed NS array, with the corresponding SAED pattern (top right) and elemental mapping (bottom right). (d) HAADF-STEM image of the hexagonally packed ND array, with the corresponding SAED pattern (top right) and elemental mapping (bottom right).

which each ND is surrounded by six NSs, while each nanosphere is coordinated by three NDs (Fig. 4a). The long-range order is confirmed by large grain sizes and the corresponding SAED pattern (Fig. 4b and Fig. S11). HAADF-STEM imaging and elemental mapping resolve that Fe_3O_4 NSs occupy the interstitial voids between adjacent NDs (Fig. 4b).

After thermal treatment, the same oxalic-acid etching protocol selectively removes one component from the dumbbell–sphere superlattice, yielding ordered NCP arrays. Preferential etching of the NDs produces a honeycomb-packed Fe_3O_4 lattice (Fig. 4c and Fig. S12),[7] whose long-range order is preserved as evidenced by SAED, while Fe mapping confirms that only Fe_3O_4 NSs remain. The Fe_3O_4 NSs size is essentially unchanged, and the interparticle spacing matches the waist dimension of the removed NDs (Fig. S12).

Conversely, reversing the etching selectivity removes the Fe_3O_4 NSs while preserving the NDs, yielding an ordered hexagonal NCP ND array, as confirmed by SAED and Gd elemental mapping (Fig. 4d). After etching, the diagonal head size decreases from 43.0 to 37.3 nm, and the initially sharp hexagonal heads become visibly more rounded, suggesting facet-selective dissolution that progressively smooths the dumbbell geometry during etching, while the overall hexagonal registry is maintained (Fig. S13). Similarly, the etching process evolves progressively with time, as evidenced by the temporal statistics in Fig. S14. This establishes a general principle: etching selectivity is governed by particle composition rather than shape. By exploiting nanoscale heat accumulation in $NaYF_4$ NPs, thermal energy is translated into ligand reconstruction and programmable interfacial chemistry, enabling reversible and morphology-independent control of etching sequences in binary superlattices.

We demonstrate a simple and controllable approach to selectively etch BNSLs. Thermally-induced reorganization and densification of the ligand shell on $NaYF_4$ NPs inverts the relative etching preference of the two components without changing the etchant. The concept's generality across different $NaYF_4$ morphologies highlights its potential as a versatile platform for nanoscale design.

This work was supported by the NSFC (52333013, 52522317, 52503361, 22025501, and 22088101) and the Shanghai Municipal Science and Technology Project (24TS1410200, 23JC1400100, 2024ZDSYS02, 24JD1400700, and 24QA2700800).

Conflicts of interest

There are no conflicts to declare.

Data availability

The data supporting this article have been included as part of the supplementary information (SI). Supplementary information is available. See DOI: https://doi.org/10.1039/d6cc00778c.

References

1 Y. Kang, X. Ye, J. Chen, Y. Cai, R. E. Diaz, R. R. Adzic, E. A. Stach and C. B. Murray, *J. Am. Chem. Soc.*, 2013, **135**, 42–45.
2 F. Schulz, O. Pavelka, F. Lehmkühler, F. Westermeier, Y. Okamura, N. S. Mueller, S. Reich and H. Lange, *Nat. Commun.*, 2020, **11**, 3821.
3 A. Dreyer, A. Feld, A. Kornowski, E. D. Yilmaz, H. Noei, A. Meyer, T. Krekeler, C. Jiao, A. Stierle, V. Abetz, H. Weller and G. A. Schneider, *Nat. Mater.*, 2016, **15**, 522–528.
4 Y. Liu, M. Klement, Y. Wang, Y. Zhong, B. Zhu, J. Chen, M. Engel and X. Ye, *J. Am. Chem. Soc.*, 2021, **143**, 16163–16172.
5 T. Udayabhaskararao, T. Altantzis, L. Houben, M. Coronado-Puchau, J. Langer, R. Popovitz-Biro, L. M. Liz-Marzán, L. Vuković, P. Král, S. Bals and R. Klajn, *Science*, 2017, **358**, 514–518.
6 K. Santhosh, O. Bitton, L. Chuntonov and G. Haran, *Nat. Commun.*, 2016, **7**, 11823.
7 M. P. Boneschanscher, W. H. Evers, J. J. Geuchies, T. Altantzis, B. Goris, F. T. Rabouw, S. A. P. van Rossum, H. S. J. van der Zant, L. D. A. Siebbeles, G. Van Tendeloo, I. Swart, J. Hilhorst, A. V. Petukhov, S. Bals and D. Vanmaekelbergh, *Science*, 2014, **344**, 1377–1380.
8 M. Piotrowski, Z. Ge, X. Han, Y. Wang, A. K. Bandela and U. Thumu, *Nanoscale*, 2023, **15**, 5188–5192.
9 Y. Cai, M. Lu, X. Qin, D. Jin and J. Zhou, *Nat. Commun.*, 2025, **16**, 4927.
10 Z. Zheng, H. Wang, Y. Gao, S. Wan, L. Lv, J. Yang, D. Yang, Y. Ling, T. Li and A. Dong, *ACS Nano*, 2025, **19**, 29788–29797.
11 A. Dong, J. Chen, P. M. Vora, J. M. Kikkawa and C. B. Murray, *Nature*, 2010, **466**, 474–477.
12 H. Hu, M. Yu, F. Li, Z. Chen, X. Gao, L. Xiong and C. Huang, *Chem. Mater.*, 2008, **20**, 7003–7009.
13 Z. Chen, H. Chen, H. Hu, M. Yu, F. Li, Q. Zhang, Z. Zhou, T. Yi and C. Huang, *J. Am. Chem. Soc.*, 2008, **130**(10), 3023–3029.
14 K. I. Hadjiivanov, D. A. Panayotov, M. Y. Mihaylov, E. Z. Ivanova, K. K. Chakarova, S. M. Andonova and N. L. Drenchev, *Chem. Rev.*, 2021, **121**, 1286–1424.
15 L. Wang and Y. Li, *Nano Lett.*, 2006, **6**, 1645–1649.
16 Z. Wang, A. S. S. Singaravelu, R. Dai, Q. Nian, N. Chawla and R. Y. Wang, *Angew. Chem., Int. Ed.*, 2020, **59**, 9556–9563.
17 N. W. Park, W. Y. Lee, J. A. Kim, K. Song, H. Lim, W. D. Kim, S. G. Yoon and S. K. Lee, *Nanoscale Res. Lett.*, 2014, **9**, 96.
18 J. M. Gonçalves, A. R. N. Bastos, S. J. L. Ribeiro, L. D. Carlos, R. L. L. Longo, J. M. A. Caiut and R. A. S. Ferreira, *Nanoscale Adv.*, 2024, **6**(5), 1486–1496.

